Prediction and Diagnosis for Unsteady Electromagnetic Vibroacoustic of IPMSMs for Electric Vehicles Considering Rotor Step Skewing and Current Harmonics

Shengsen Zhou[1], Conggan Ma[1*], Nic Zhang[2], Yue Guo[3], MicheleDegano[4], Chris Gerada[4], Feifei Bu[5], Jinling Zeng[6], Qiongyao Li[1] and Yuansheng An[1]

[1*]School of Automotive Engineering, Harbin Institute of Technology-Weihai, Yiyuan, Weihai, 264209, Shandong, China.
[2]Department of Mechanical Engineering, University of Bath, Claverton Down, Bath, BA2 7AY, UK.
[3]Coventry University, Priory Street, Coventry, CV1 5FB,UK.
[4]Power Electronics, Machines and Control research group, University of Nottingham, University Park, Nottingham, NG7 2RD,UK.
[5]Nanjing University of Aeronautics and Astronautics, Yudao, Nanjing, 210016,China.
[6]Advanced Technology Lab, Shanghai XPT Technology Co.Ltd., Anting, Shanghai, 201804,China.

*Corresponding author(s). E-mail(s): mcg@hit.edu.cn;
Contributing authors: 20b908148@stu.hit.edu.cn; qz254@bath.ac.uk; yue.guo@coventry.ac.uk; michele.degano@nottingham.ac.uk; chris.gerada@nottingham.ac.uk; bufeifei1984@163.com; janny.zeng@nio.com; 19b908147@stu.hit.edu.cn; 20b908147@stu.hit.edu.cn;

Abstract

Purpose: This study provides a detailed investigation on the prediction and diagnosis of unsteady electromagnetic vibroacoustic performance of IPMSMs for electric vehicles under typical unsteady operating conditions with consideration of rotor step skewing and current harmonics.
Methods: Firstly, the control model considering the influence of PWM carrier modulation and rotor step skewing is established. Based on this, the currents of the IPMSM under unsteady operating conditions (driving condition and feedback braking condition) are obtained. Accordingly, the currents calculated through the control model are used as the excitation source of electromagnetic finite element. Then, the electromagnetic vibroacoustic performance under unsteady operating conditions is calculated through electromagnetic force subsection mapping and acoustic transfer vector (ATV) method. Moreover, the conditions where resonance vibroacoustic occurs are diagnosed. Finally, the results of prediction and diagnosis are fully verified by experiments of multiple physical fields.
Results and Conclusions: The amplitude errors between prediction results and test results are less than 3.2%. The influence of current harmonics on electromagnetic vibroacoustic can be predicted. The frequency range and speed range of predicted peak vibroacoustic are consistent with the experimental results. The rotor step skewing can be used to weaken the vibroacoustic amplitude of IPMSMs under typical unsteady conditions in the full speed range.This study provides guidance for prediction and diagnosis for electromagnetic vibroacoustic performance of IPMSMs under typical unsteady operating conditions.

Keywords: Unsteady operating conditions, IPMSMs, rotor step skewing, electromagnetic vibroacoustic

1 Introduction

IPMSMs are widely used as traction motors for electric vehicles thanks to their reluctance torque component and high power density. To achieve superior vibroacoustic quality, the vibroacoustic of IPMSMs should be reduced according to the prediction and diagnosis in the early stage of the motor design. Therefore, prediction and diagnosis of electromagnetic vibroacoustic has gradually become an important aspect in motor design.

The prediction method of electromagnetic vibroacoustic can be divided into numerical[1–13], analytical[14, 15], and semi-analytical methods [14, 16] depending on the calculation types. It can also be divided into single speed and variable speed conditions [10, 14]. Analytical or semi-analytical methods are often used to calculate electromagnetic vibroacoustic under variable speed conditions due to their higher computational efficiency. In [14], the electromagnetic vibroacoustic of the axial flux permanent magnet synchronous motor (AFWM) was predicted analytically. In [16], a piecewise first-order linear function was proposed to calculate the total peak acceleration and the radial vibration of the switched reluctance motor. These works shown the effectiveness of analytical models for predicting vibroacoustic . However, it is very difficult to ensure the accuracy of the analytical results of multi-physical quantities of IPMSMs such as electromagnetic force, structural modals, vibration, and vibroacoustic . It is because of the complex geometry, the nonlinearity and high saturation of materials of the IPMSMs.

Numerical method can be used to accurately calculate the multi-physical quantities of IPMSMs with complex structure and working conditions. In[4, 5, 8], the electromagnetic vibroacoustic of the switched reluctance motor was calculated through multi-physics numerical simulation. In [6, 7, 11, 17], multi-physics numerical prediction models of IPMSMs vibroacoustic were proposed. The above works shown that numerical method can predicted steady vibroacoustic accurately. However, compared to other general industrial application scenarios, electric vehicles are in the frequent stop-start, quick acceleration and regen brake events during a driving cycle [18]. Thus, IPMSMs are often operating at unsteady conditions of variable speeds and variable torque, which can cause the excitation force frequency to cross the modal frequency of the IPMSMs during the driving cycle. As a result, the resonance electromagnetic vibroacoustic in the full speed range of driving cycle is inevitable. Therefore, the vibroacoustic prediction at a single operating point cannot be used to evaluate where the peak vibroacoustic occurs. Using the acoustic transfer vector (ATV) method, meanwhile, can reduce the calculation time of multi-speed vibroacoustic and speed up the calculation process. Therefore, in [10], the authors used the ATV method to calculate unsteady electromagnetic vibroacoustic of SPMSMs under the starting conditions with multi-speed point.

At early design stage, neither the prototype nor the experimental results are available. Nevertheless, the existing prediction models depend on produced prototypes and test results. Therefore, electromagnetic vibroacoustic still cannot be implanted into the design process. The control model can be used to simulate various unsteady processes. The stator current can also be obtained from it as input for electromagnetic calculations. In this way, the entire flow of vibroacoustic simulation considering the unsteady operating processes can be realized at early design stage. However, high-precision control models are rarely considered in the vibroacoustic prediction process, especially for IPMSMs with rotor step skewing and magnetic saturation.

In addition, electromagnetic vibroacoustic does not have a completely linear relationship with the speed in the unsteady conditions[2]. The resonance vibroacoustic has the largest peak value in the entire speed range, which greatly affects the motor quality and causes passengers to complain. Therefore, it is of great significance to diagnose the frequency band or speed range where peak resonance vibroacoustic is prone to occur at early design stage, especially for IPMSMs used for driving electric vehicles. The black-box method is generally used to diagnose the peak resonance vibroacoustic [2, 12]. However, it depends on the vibroacoustic experiment of motors.

More importantly, to provide guidance to further reduce the resonance vibroacoustic, the electromagnetic excitation source of resonance vibroacoustic needs to be diagnosed.

To overcome the existing challenges, the prediction and diagnosis for unsteady electromagnetic vibacoustic of ISPMSMs are studied in detail

in this paper. The contribution of this paper is the proposed method for predicting and diagnosing unsteady electromagnetic vibroacoustic of IPMSMs for electric vehicles. Unlike previous research, the proposed method considers the rotor step skewing, the PWM harmonic current of the controller, and different unsteady operating conditions (acceleration and feedback braking).

This article is organized as follows: In Section 2, the flowchart of the prediction and diagnosis for unsteady electromagnetic vibroacoustic of IPMSMs is introduced, where the rotor step skewing is considered. In Section 3, the prediction model for unsteady electromagnetic vibroacoustic of IPMSMs are established, which consists of a control model, an electromagnetic finite element model and a structural finite element model. In Section 4 the distribution characteristics of electromagnetic force and vibroacoustic with and without the rotor step skewing are investigated under unsteady conditions. The peak vibroacoustic conditions and the source of the excitation force are determined. In Section 5, the results of prediction and diagnosis are fully verified by experiments of multiple physical fields.

2 Prediction-Diagnosis Process for Unsteady Electromagnetic Vibroacoustic

The flowchart of the proposed prediction-diagnosis method is shown in Fig.1. It mainly consists of 6 steps:

(1) The d- and q-axis inductance map of the IPMSM with step skewing as a motor/generator running under different i_d-i_q combinations are calculated by electromagnetic finite element (FE) software. The inductance parameters that vary with the current are applied to the simulation model of the IPMSM.

(2) Stator current obtained from the control model is supplied as excitation source to n-segment 2D electromagnetic FE models with different initial angles of the rotor, where n is the number of axial segments. Then, the electromagnetic force distribution on electromagnetic FE nodes in each segment is obtained.

(3) 3D geometric model of the IPMSM is established. Considering anisotropy of stator core and winding materials, structural FE model of prototype is set to calculate the natural modal shapes of the stator assembly and the whole machine.

(4) 2D electromagnetic force is extended to 3D and transferred to the structural FE grid in each segment. At the same time, modal information is imported into vibration response model. Then, vibration response is calculated by the modal superposition method (MSM).

(5) Vibroacoustic response under unsteady working conditions is calculated using the presolved acoustic transfer vector (ATV).

(6) By using predicted results, the frequency band or speed range where peak resonance vibroacoustic is prone to occur is diagnosed. By analyzing unsteady electromagnetic force and simulation modal, the electromagnetic excitation source of resonance vibroacoustic is diagnosed.

3 Prediction of Unsteady Electromagnetic Vibroacoustic

The rotor step skewing is equivalent to the superposition of multiple segments rotors with different initial rotor angles, as shown in Fig.2. An 8-pole 48-slot IPMSM with the rotor step skewing for electric vehicle driving cycle is considered as a case study. The key parameters are shown in Table 1.

Table 1 Main parameters of the IPMSM

Parameter	Symbol	Value	Unit
Inner diameter of stator core	R_s	71.8	mm
Outer diameter of rotor core	R_r	71.0	mm
Number of poles	p	8	–
Number of slots	Q	48	–
Number of axial segments	n	6	–
Total angle of oblique pole	β	7.5	0

3.1 Control Model of IPMSM

Accelerating and feedback braking are two typical unsteady operating conditions of electric vehicles. Considering the above, IPMSMs work in positive driving mode and positive braking mode, respectively. The two modes cover common unsteady working conditions such as starting, accelerating, feedback braking and idling coasting. Considering the complex driving conditions, a control model is established, as shown in Fig.3.

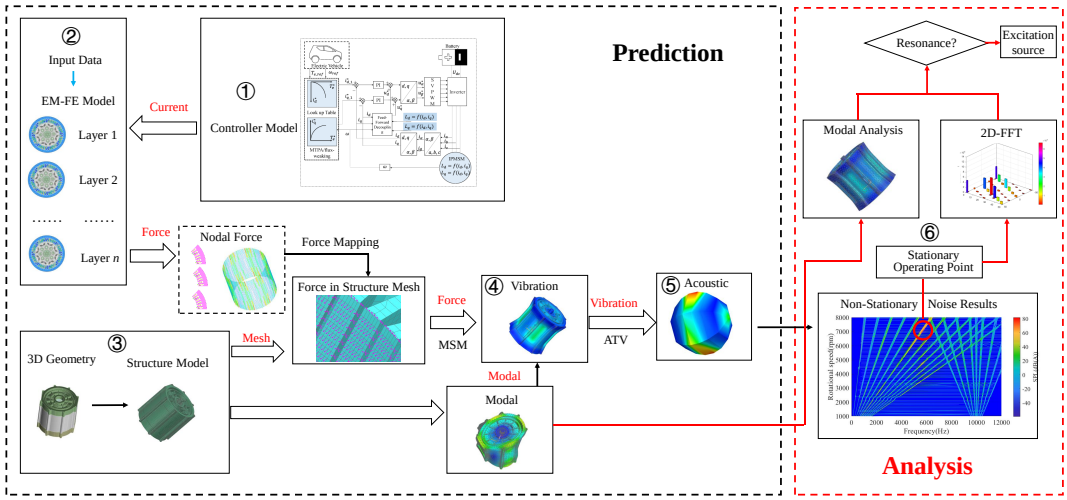

Fig. 1 Flowchart of the prediction and diagnosis for unsteady electromagnetic vibroacoustic of IPMSMs considering the rotor step skewing

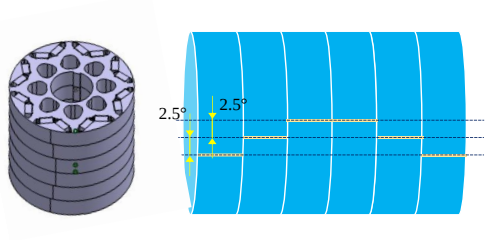

Fig. 2 Schematic diagram of rotor step skewing

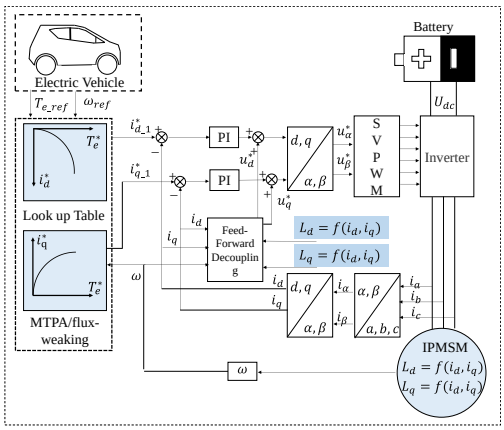

Fig. 3 Control model of IPMSM

Due to the complex magnetic circuit structure, serious magnetic saturation and a large range of current changes during the unsteady operating process, the IPMSM parameters exhibit nonlinear characteristics, which vary with the current. Therefore, an inductance-based parameter estimation method with high accuracy, high adaptability and independent of bench test parameters is selected.

The d- and q-axis inductance map of the IPMSM with step skewing as a motor/generator running under different i_d-i_q combinations are calculated by electromagnetic finite element software, as shown in Fig.4.

The nonlinear inductance characteristics under different unsteady conditions can be better depicted by calculating the d, q-axis inductance values under different current pairs. As a result, high precision simulated currents can be obtained. That is, to obtain more accurate inductance curve and simulation current, a large range and a large number of current pairs are required. In this paper, the range of current pairs are set as:-750A< i_d <0, -750A< i_q <750A. The steps of current pairs are set as 50A.

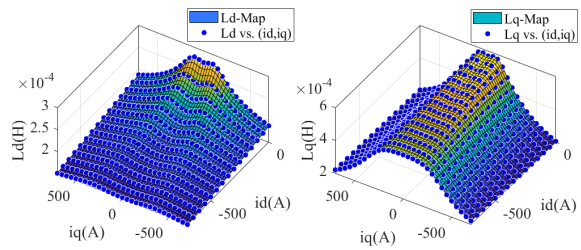

(a) (b)

Fig. 4 d- and q-axis inductance map

Then, the inductance parameters that vary with the current are applied to the control model of the IPMSM, which contains coordinate transformation equation, current state equation (1)-(4), torque equation (5) and motion equation (6). The rotor step skewing, magnetic saturation and cross-coupling characteristics of the IPMSMs can be simulated accurately by using this method.

$$\psi_d\left(i_d, i_q\right) = L_d\left(i_d, i_q\right) i_d + \psi_f\left(i_d, i_q\right) \tag{1}$$

$$\psi_q\left(i_d, i_q\right) = L_q\left(i_d, i_q\right) i_q \tag{2}$$

$$u_d\left(i_d, i_q\right) = R_s i_d + \frac{\mathrm{d}\psi_d}{\mathrm{d}t} - \omega_e \psi_q \tag{3}$$

$$u_q\left(i_d, i_q\right) = R_s i_q + \frac{\mathrm{d}\psi_q}{\mathrm{d}t} + \omega_e \psi_d \tag{4}$$

$$T_e\left(i_d, i_q\right) = \frac{3}{2} n_p \left[\psi_d i_q - \psi_q i_d\right] \tag{5}$$

$$T_e\left(i_d, i_q\right) - T_1 = \frac{J}{n_p} \frac{\mathrm{d}\omega}{\mathrm{d}t} \tag{6}$$

where ψ_d, ψ_q, L_d, L_q, i_d, i_q, u_d, u_q are flux linkage, inductance, current and voltage in d-and q-plane, respectively. R_s is stator resistance, ω_e is rotational speed, n_p is the number of pole pairs, T_e is electromagnetic torque, T_1 is load torque, J is moment of inertia.

The Simulation results under two typical working conditions are shown in Fig.5. In the full speed range, the variable parameter IPMSM model and the control model based on look-up tables have good static and dynamic characteristics.

The frequency domain distributions of simulation currents are shown in Fig.6. It can be seen that the current amplitude under braking condition is lower than that under accelerating condition. Besides, the current generally contains three types of components: fundamental wave f_c, low-order odd multiple harmonic $(6h \pm 1)\ f_c$ and high-frequency sideband harmonics $f_s \pm k f_c$ near the switching frequency f_s.

Taking acceleration conditions as an example, the comparison of torque-speed characteristics of the variable parameter model, the fixed parameter model and the experimental results is shown in Fig.7. When the variable parameter IPMSM control model is adopted, the rotor step skewing and magnetic saturation can be considered, the torque output capacity of the IPMSM at high-speed conditions is improved.

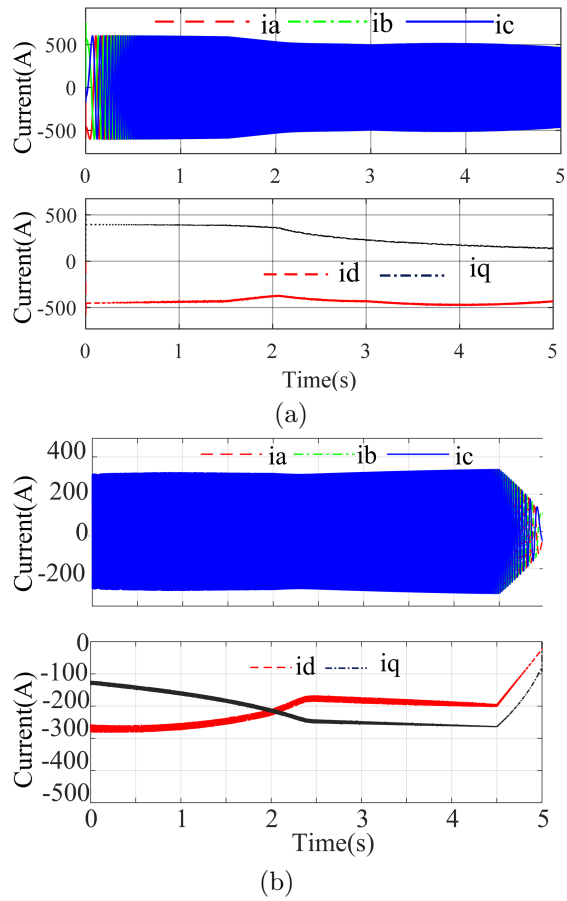

Fig. 5 Simulation results of the control model (a) Stator current under accelerating condition, (b) Stator current under braking condition

3.2 Modal Analysis

The stator assembly is the direct excitation object of electromagnetic force, which contains stacked cores and stacked windings. Due to the large number of finite element units, it is not feasible to implement geometric modeling and finite element analysis of the actual structure. Therefore, the anisotropy of materials can be used to equivalent the anisotropy of structures in simulation modal analysis.

Multilayer and distributed windings are generally used in IPMSMs for electric vehicles to enhance the sinusoidal characteristics of armature magnetomotive force. The longer end is the characteristic of this kind of winding, so it cannot be ignored in the simulation modal analysis. In the existing researches, methods such as including the winding mass in the core method, establishing a

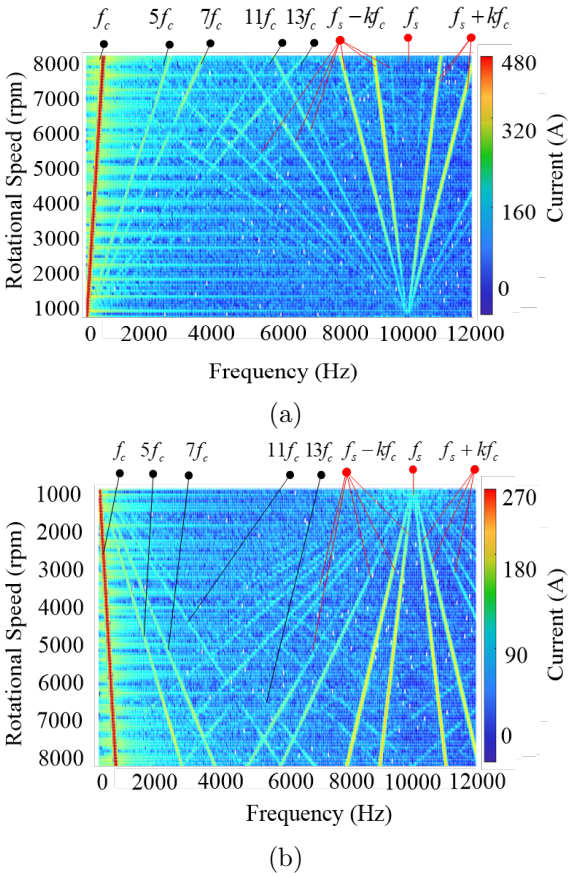

Fig. 6 A-phase current time-frequency diagram: (a) Under accelerating condition, (b) Under braking condition

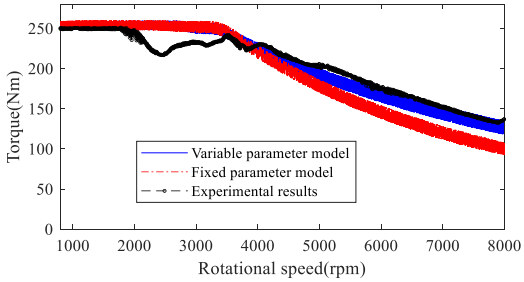

Fig. 7 Comparison of variable parameter model, fixed parameter model and experimental results

conductor-based winding method, and including the winding mass in the end method are used to equivalent the influence of the winding on the stator assembly mode. Compared with including the winding mass in the core, the equivalent end ring can be used to better simulate the influence of the end winding; compared with the conductor-based winding method, the equivalent end ring modeling is simpler, the number of finite elements is lower, and the calculation speed is faster. Therefore, in this paper, the equivalent end ring is used to represent the influence of the winding on the stator assembly modal.Adhesion conditions are used for face-to-face contact. It is shown in Fig. 8.

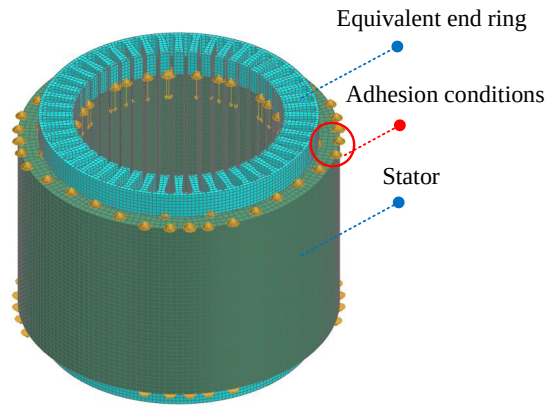

Fig. 8 The contact of winding and stator

Anisotropic materials are defined by 9 engineering constants of three orthogonal symmetry planes, namely E_x, E_y, E_z, G_{xy}, G_{yz}, G_{zx}, μ_{xy}, μ_{yz}, and μ_{zx}. Among them, xy, yz, and xz represent different planes, x, y, and z represent different coordinate axis directions, μ, E, and G represent Poisson's ratio, Young's modulus, and shear modulus, respectively. The influence of Poisson's ratios on stator modal frequency can be ignored, so the Poisson's ratios in the three planes of the core material are the same as that of the silicon steel sheet. According to the actual core compression characteristics, the Young's modulus in the x and y directions are equal, and the shear modulus in the yz plane and zx plane are equal. Therefore, eight independent anisotropic material parameters for stator core and equivalent end ring need to be determined, which can be identified by experimental modal analysis [13].

In order to determine the material anisotropy parameters and verify the accuracy of the equivalent model, modal tests of the stator assembly are carried out. 12 acceleration sensors are arranged along the circumference of the whole stator assembly, and two layers are arranged along the axis. As shown in Fig 9, hammering method is used to test modal parameters. The response signals are transmitted to the data acquisition and signal

processing (DASP) analyzer produced by China Orient Institute of Noise & Vibration.

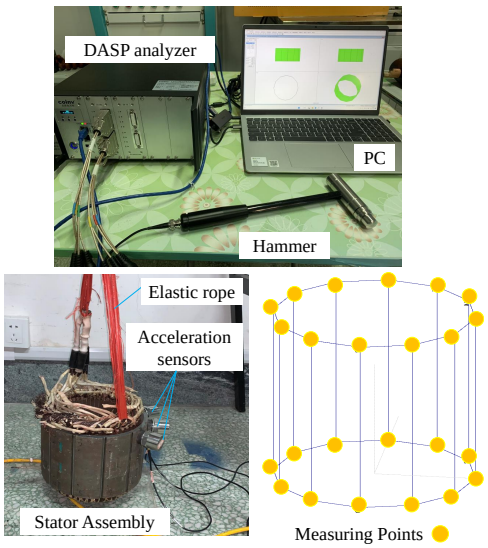

Fig. 9 Experimental equipment and measuring points for experimental modal analysis

In order to improve the accuracy of the simulation modal analysis, according to the measured modal frequency of the stator assembly, the values of the independent material anisotropy parameters of the stator core and the equivalent end ring are optimized. The optimization goal is to minimize the error between the calculated modal frequency and the experimental frequency. The optimized parameters are shown in Table 2.

Table 2 Orthotropic material parameters

	Density (kg/m^3)	Poisson's ratio	Young's modulus	Shear modulus
stator	7750	0.3	$E_x\,(E_y) = 64$GPa $E_z = 200$GPa	$G_{xy} = 70$GPa $G_{yz}\,(G_{zx}) = 14$GPa
winding	5144	0.3	$E_x\,(E_y) = 60$GPa $E_z = 200$GPa	$G_{xy} = 0.77$GPa $G_{yz}\,(G_{zx}) = 1.5$GPa

The comparative verification of modal shape and frequencies of stator assembly are shown in Table 3 and Table 4 respectively. The experimental results show that the maximum error of the calculated modal analysis in this paper is less than 4%, which meets the actual needs of the project.

Table 3 Modal shapes of stator assembly

Modal shape	$(2,0)$	$(2,1)$	$(3,0)$
Test	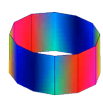	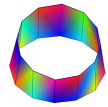	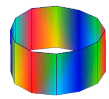
Simulation	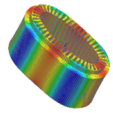	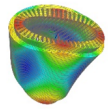	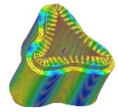
Modal shape	$(3,1)$	$(4,0)$	$(0,0)$
Test	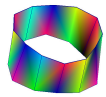	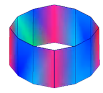	
Simulation	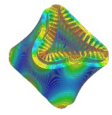	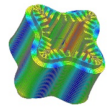	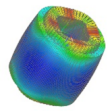

Table 4 Modal frequencies of stator assembly

Modal shape	$(2,0)$	$(2,1)$	$(3,0)$	$(3,1)$	$(4,0)$	$(0,0)$
Modal frequency of test(Hz)	694	869	1854	2023	3109	5589
Modal frequency of simulation(Hz)	672	835	1799	1948	3011	5542
Relative error(%)	3.17	3.91	2.97	3.71	3.15	0.84

3.3 Calculation and Mapping of Electromagnetic Force

To calculate the electromagnetic force, the currents are supplied as excitation source for electromagnetic FE model. Firstly, the unsteady process is discretized into a finite number of steady operating conditions. Then, the electromagnetic force of each steady-state speed operating condition is calculated. The mapping process of electromagnetic force is as follows:

Firstly, according to the periodicity of the motor, a 1/8 electromagnetic finite element model is established. The electromagnetic force on the finite element mesh of the stator tooth surface is extracted and expanded to the entire circumference. Then, the electromagnetic force of each segment is stretched in the axial direction and mapped to the of the structure finite element mesh, as shown in Fig. 10. For the IPMSMs without step skewing, only the force on the electromagnetic finite element grid within a segment

needs to be expanded and mapped to the entire axial stator tooth surface.

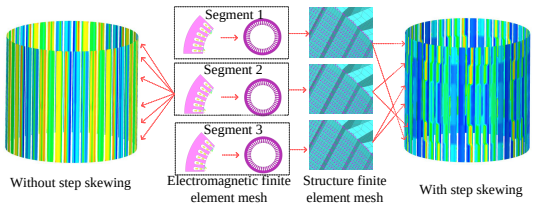

Fig. 10 Segmented mapping of electromagnetic force

3.4 Prediction of Unsteady Electromagnetic Vibroacoustic

Completely continuous unsteady vibroacoustic should be simulated in the time domain. However, to calculate the vibroacoustic with the upper frequency limit of 12000 Hz, the time step should be at least 4×10^{-5}s. If the total solution time is 5 s as Fig. 5, 1.25×10^{5} steps need to be calculated. This is unacceptable for the early design analysis of the IPMSM. Therefore, using the idea of short-time Fourier transform (STFT) for reference, the continuous unsteady signal can be discretized into multiple finite-time stationary signals. ATV represents the mapping relationship between vibration and vibroacoustic , which is suitable for efficient calculation of vibroacoustic under multiple operating conditions. It has been widely used in engine and other products[10]. In order to efficiently predict unsteady vibroacoustic at the early stage of motor design, 100 rpm is set as the step size to discrete the continuous unsteady process. The expression is shown in (7)[10]:

$$pr(f) = \{\mathrm{ATV}(f)\}^{\mathrm{T}}\{v_n(f)\} \tag{7}$$

where, $pr(f)$ is the field point sound pressure. f is the frequency. $v_n(f)$ is the normal vibration speed of the motor surface.

The calculation results of unsteady electromagnetic vibroacoustic during the accelerating process are shown in Fig. 11. The following characteristics are concluded:

- The main frequency components are $2kf_c$, which appear as unidirectional rays. The other part is high frequency sideband harmonic $f_s \pm kf_c$, which is bidirectional umbrella shape near the switching frequency f_s.
- The predicted peak vibroacoustic appears in the frequency range (5110 Hz-6080 Hz) with the speed range (6300 rpm-7600 rpm), which is located in the resonance band caused by the (0,0) and (0,1) order breathing modal. The maximum vibroacoustic occurs at the rotational speed 7100 rpm.
- The application of the rotor step skewing has a significant reduction effect on the peak vibroacoustic . The maximum vibroacoustic is reduced from 90.52 dB(A) to 88.15 dB(A).

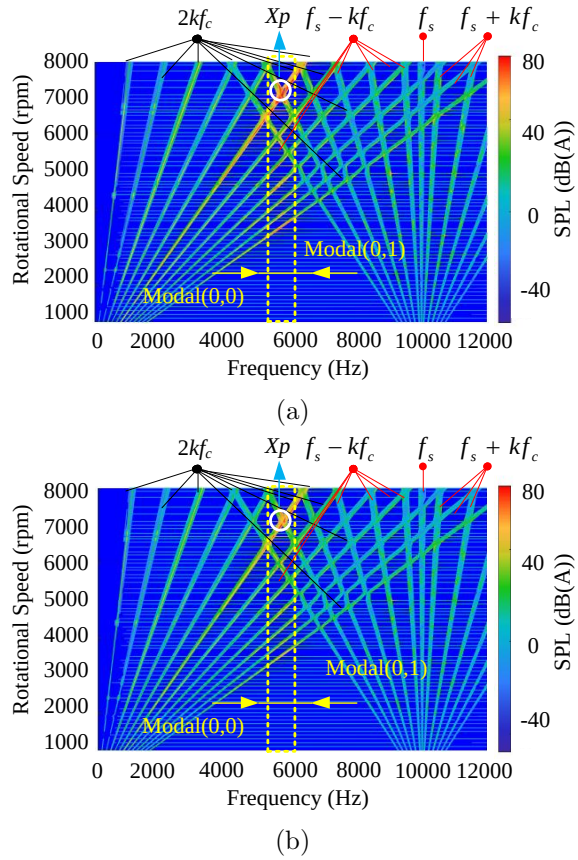

Fig. 11 Time-frequency diagram of electromagnetic vibroacoustic under accelerating condition: (a) Without skewing, (b) With skewing

In the full speed and full frequency range, the peak vibroacoustic of the braking condition is lower than that of accelerating condition, as shown

in Fig. 12. The frequency components and the predicted point of peak vibroacoustic are the same as that of accelerating condition.

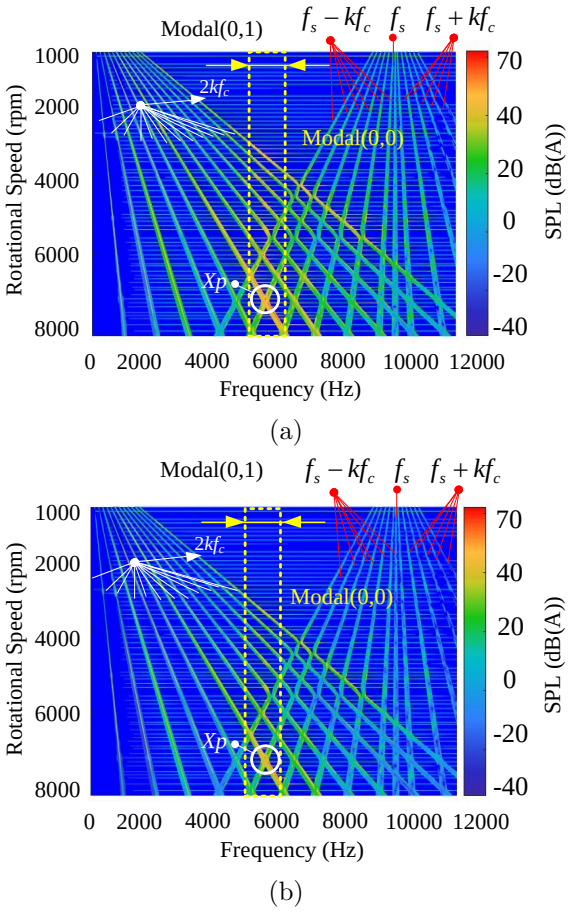

Fig. 12 Time-frequency diagram of electromagnetic vibroacoustic under braking condition: (a) Without skewing, (b) With skewing

3.5 Mechanism analysis of electromagnetic vibroacoustic

In order to analyze the frequency characteristics of electromagnetic noise, the air gap magnetic field expression of IPMSMs is derived by magnetic potential method and linear superposition method[14], as shown in (8). The purpose of analytical derivation is to analyze the mechanism source of electromagnetic vibration noise rather than to calculate accurately, so the material nonlinearity, magnetic steel saturation and slotting effect are ignored.

$$\begin{aligned} B_r(\theta,t) &= B_{mr}(\theta,t) + B_{ar}(\theta,t) \\ &= \sum_{n=1,3,5,\ldots}^{\infty} B_n \cos\left(np\theta - 2\pi n f_c t\right) \\ &+ \sum_{z=1}^{\infty}\sum_{\eta=1}^{\infty} B_{\eta z} \cos\left(\eta p\theta - 2\pi s_z f_z t + \theta_z\right) \end{aligned} \tag{8}$$

where B_{mr} and B_{ar} are permanent magnetic field and armature magnetic field respectively, B_n is the n-th harmonic amplitude of permanent magnetic field, $B_{\eta z}$ is the harmonic amplitude of armature magnetic field with spatial order η and frequency order z, s_z is the positive and negative polarity of the armature magnetic field with frequency order z, θ_z is the phase angle of the armature magnetic field with frequency order z.

Radial electromagnetic force waves are the main excitation source of electromagnetic vibration of IPMSMs for electric vehicles, and their frequency characteristics are consistent with those of electromagnetic noise. Therefore, only the radial electromagnetic force wave is analyzed in analytical derivation, as shown in (9).[4]

$$P_r(\theta,t) = \frac{B_r^2 - B_t^2}{2\mu_0} \tag{9}$$

where P_r and B_t are radial electromagnetic force wave and tangential air gap magnetic density, respectively. B_t is much smaller than B_r, so it is ignored in the formula of radial electromagnetic force wave. (9) can be further simplified as[4]:

$$P_r(\theta,t) = \frac{B_r^2}{2\mu_0} \tag{10}$$

Substitute (8) into (10) to get (11)[4]. The source, spatial order and frequency characteristics of radial electromagnetic force wave can be obtained from (11). It is also shown in Table 5. When the angular velocity in (11) is unsteady, the unsteady electromagnetic force can be obtained. The unsteady speed does not affect the spatial order characteristics, nor does it add frequency components of P_r.

As shown in (11) and Table 5, the electromagnetic force sources of IPMSMs mainly fall

Table 5 Source and characteristics of radial electromagnetic force wave

Sources	Spatial order	Frequency characteristic
B_{mr}^2	$(n_1 \pm n_2)\, p$	$(n_1 \pm n_2)\, f_c$
B_{ar}^2	$(\eta_1 \pm \eta_2)\, p$	$s_{z_1} f_{z1} \pm s_{z_2} f_{z2}$
$B_{mr} \times B_{ar}$	$(n \pm \eta)p$	$nf_c \pm s_z f_z$

into three categories: (1) The function of permanent magnet magnetic field; (2) The function of armature reaction magnetic field; (3) Interaction between permanent magnet magnetic field and armature reaction magnetic field.

The main excitation source of electromagnetic noise is the first and third items in Table 5. Among them, the current harmonics mainly affect the third item. The frequency characteristics of electromagnetic force waves are summarized as follows:

(1) With the function of permanent magnet magnetic field, since n_1 and n_2 are both odd numbers, the frequencies of P_r are even times of the fundamental wave frequency f_c, i.e., $2kf_c$, k=1,2,3...;

(2) With sine current wave f_c and odd times current harmonics $(6h \pm 1)f_c$, $z = 6h \pm 1$ is an odd number, and n is also an odd number. Hence, the frequencies of P_r are also even times of the fundamental wave frequency f_c, i.e., $2kf_c$, k=1,2,3...;

(3) With high-frequency sideband harmonic current, the frequency components of electromagnetic force waves are $k_1 f_s \pm (k_2 \pm n)\, f_c$.

Analysing the spatial order characteristics of electromagnetic force waves in Table 3, the following conclusions are drawn: For motors with integral slot distribution, $\eta = 6r \pm 1$ is an odd number and n is an odd number, so the spatial order can be written as $2kp \pm mQ$, where m is a natural number.

4 Diagnosis of Electromagnetic Force

4.1 Analysis of Unsteady Electromagnetic Force

The radial electromagnetic force acting on the stator tooth surface during IPMSM operation is the main cause of the electromagnetic vibroacoustic . Therefore, the unsteady distributions of electromagnetic forces are analyzed first.

According to[19], the deformation of the stator can be expressed as:

$$Y_0 = -\frac{r_{\mathrm{i}} N}{Eh}\sigma_{\mathrm{rad},0} \tag{12}$$

$$Y_1 = \frac{4}{3}\frac{r_{\mathrm{i}} l}{E\left(\frac{d}{L}\right)^4 L}\sigma_{\mathrm{rad},1} \tag{13}$$

$$Y_{s>=2} = Y_0\left(\frac{2\sqrt{3}N}{h}\frac{1}{s^2-1}\right)^2 \sigma_{\mathrm{rad},s} \tag{14}$$

where Y_s is the amplitude of the s-th order stator deformation, σ is the radial electromagnetic force density, s is the spatial order of radial electromagnetic force density, h is the radial thickness of the stator yoke, l is the axial length of the stator, d is the shaft diameter, and L is the distance of the bearings, E is Young's modulus of the stator, r_i and N are the inner and average radius of the stator yoke, respectively.

As can be seen from (13), for the electromagnetic force with a spatial order greater than 1, the deformation of the motor stator is inversely proportional to the fourth power of the spatial order. Therefore, the non-zero-order electromagnetic force in spatial has a very small influence on motor vibroacoustic. For the 8-pole 48-slot IPMSM, the lowest non-zero spatial harmonic of the electromagnetic force is 8-th order, as shown in Fig. 13. Hence, the spatial-zero-order electromagnetic force under the unsteady process are extracted.

Taking acceleration conditions as an example, the calculation and analysis process of electromagnetic force is as follows:

(1) The spatial and temporal distribution of the electromagnetic force on the entire tooth surface were extracted, as shown in Fig. 14.

(2) The spatial and temporal decomposition of the electromagnetic force is conducted using a method of two-dimensional Fourier transform (2D-FFT). The 2-D FFT method here is expressed as:

$$P_r(r,f) = \int_{-\infty}^{+\infty}\int_{-\infty}^{+\infty} P_r(\theta,t)e^{-j2\pi(r\theta+ft)}d\theta dt \tag{15}$$

where Pr is the radial electromagnetic force. According to it, the harmonic electromagnetic force with different spatial order and frequency order can be derived, as shown in Fig. 13.

$$
\begin{aligned}
&P_r(\theta,t)\\
&=\frac{1}{2\mu_0}\left[B_{ar}(\theta,t)+B_{nr}(\theta,t)\right]^2\\
&=\left[\sum_{n=1,3,5,\ldots}^{\infty}B_n\cos\left(np\theta-2\pi nf_ct\right)+\sum_{z=1}^{\infty}\sum_{\eta=1}^{\infty}B_{\eta z}\cos\left(\eta p\theta-2\pi s_zf_zt+\theta_z\right)\right]^2\\
&=\frac{1}{4\mu_0}\left\{\begin{array}{l}
\sum_{n_1=1,3,5,\ldots n_2=1,3,5,\ldots}^{\infty}B_{n_1}B_{n_2}\left\{\begin{array}{l}\cos\left[\left(n_1+n_2\right)p\theta-2\pi\left(n_1+n_2\right)f_ct\right]\\+\cos\left(n_1-n_2\right)p\theta-2\pi\left(n_1-n_2\right)f_ct\end{array}\right\}\\
+\sum_{n=1,3,5,\ldots}^{\infty}\sum_{z=1}^{\infty}\sum_{\eta=1}^{\infty}B_nB_{\eta=2}\left\{\begin{array}{l}\cos\left[(n+\eta)p\theta-2\pi\left(nf_c+s_zf_z\right)t+\theta_z\right]\\+\cos\left[(n-\eta)p\theta-2\pi\left(nf_c-s_zf_z\right)t-\theta_z\right]\end{array}\right\}\\
+\sum_{z_1=1}^{\infty}\sum_{n_1=1}^{\infty}\sum_{z_2=1}^{\infty}\sum_{\eta_2=1}^{\infty}B_{n_{1-1}}B_{\eta_2=2}\left\{\begin{array}{l}\cos\left[\left(\eta_1+\eta_2\right)p\theta-2\pi\left(s_{z1}f_{z_1}+s_{z_2}f_{z2}\right)t+\left(\theta_{z_1}+\theta_{z_2}\right)\right]\\+\cos\left[\left(\eta_1-\eta_2\right)p\theta-2\pi\left(s_{z1}f_{z_1}-s_{z_2}f_{z2}\right)t+\left(\theta_{z_1}-\theta_{z_2}\right)\right]\end{array}\right\}
\end{array}\right\}
\end{aligned}
\tag{11}
$$

(3) 100rpm is set as the step size. The electromagnetic force of each speed under acceleration conditions is calculated according to the above steps. Finally, the frequency characteristics of the spatial-zero-order in the entire speed range is obtained, as shown in Fig. 15 and Fig. 16.

It can be seen from Fig. 15 and Fig. 16 that the $12f_c$ is the prominent component of the electromagnetic forces under the unsteady process, which is the same as the electromagnetic vibroacoustic distribution. To compare the weakening effect of the rotor step skewing in the whole speed range, the electromagnetic forces $(0,12f_c)$ are extracted, as shown in Fig. 17. The change of the amplitude of $(0,12f_c)$ has the same trend as electromagnetic torque in the whole speed range, as shown in Fig. 7. The weakening effect of the rotor step skewing exists in the whole speed range, which means that the application of the rotor step skewing can be used to weaken the electromagnetic vibroacoustic in any speed condition, especially in the resonance frequency band excited by the electromagnetic forces $(0,12f_c)$.

4.2 Diagnosis of the Excitation Source of Resonance Vibroacoustic

There are two essential conditions for the occurrence of resonance. Firstly, the frequency of excitation force is close to natural modal frequency of the IPMSM. Secondly, the spatial order of

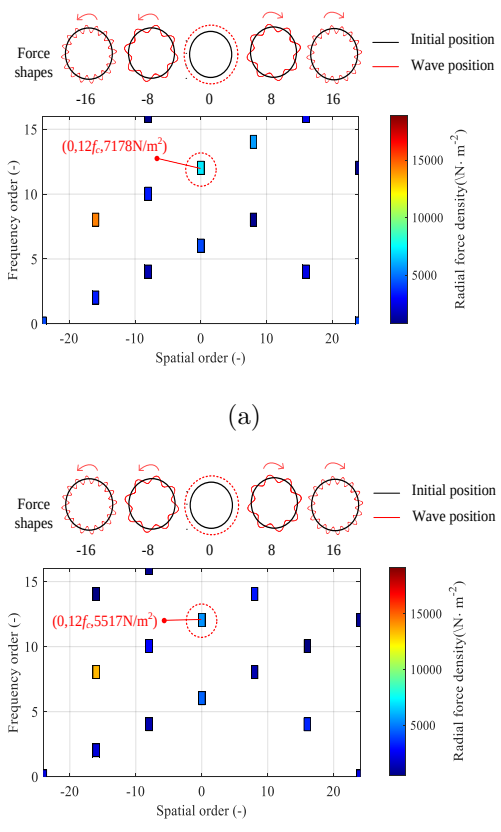

Fig. 13 Harmonic distribution of radial electromagnetic force of IPMSM: (a) Without rotor step skewing, (b) With rotor step skewing

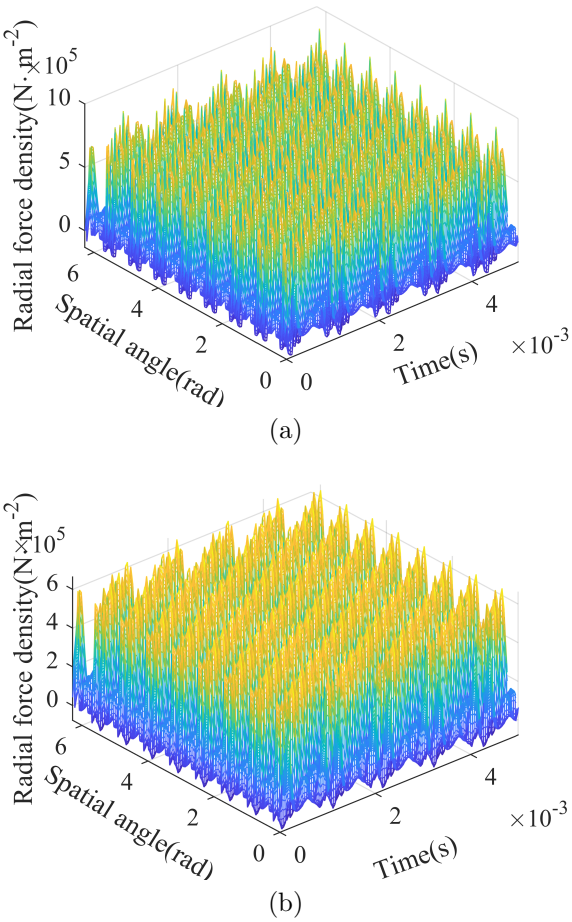

Fig. 14 The spatial and temporal distribution of the electromagnetic force: (a)Without rotor step skewing, (b) With rotor step skewing

the excitation force is consistent with the modal shape.

The frequency span of the harmonic electromagnetic force is large. It shows a ray-like distribution in the unsteady state process, which can be seen from Fig. 15, Fig. 16 and Fig. 18. Modal is the inherent property of IPMSMs and does not change with speed. Therefore, it presents a distribution perpendicular to the frequency axis, which can be seen from the green line in Fig. 18. Hence, the electromagnetic force must have intersections with some modal frequencies in the unsteady state process, as shown in the yellow circles in Fig. 18. However, resonance does not occur at all intersection positions. The process of diagnosing the excitation source is as follows:

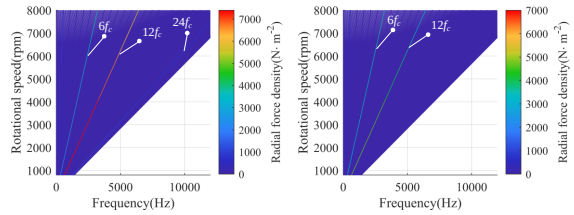

Fig. 15 Time-frequency diagram of electromagnetic vibroacoustic under accelerating condition: (a) Without skewing, (b) With skewing

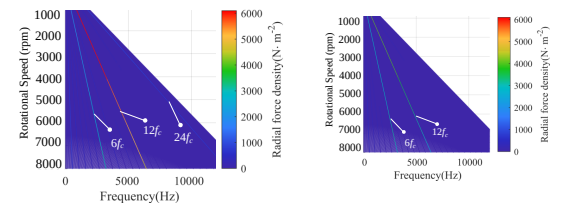

Fig. 16 Time-frequency diagram of electromagnetic force under braking conditions: (a) Without skewing, (b) With skewing.

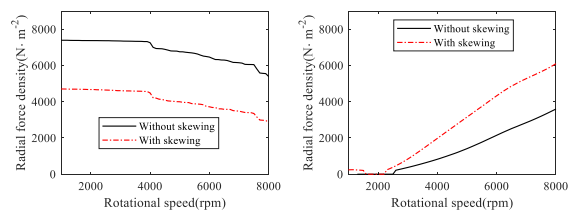

Fig. 17 (0,12fc) electromagnetic force under unsteady-state conditions: (a) Accelerating condition, (b) Braking condition

First of all, the harmonic characteristics of the electromagnetic force are analyzed. The decomposition process of electromagnetic force has been described above. For the 8-pole 48-slot IPMSM, the non-zero-order electromagnetic force in spatial has a very small influence on motor vibroacoustic. Hence, spatial-zero-order electromagnetic force has been extracted under the unsteady process, as shown in Fig. 18.

Then, several main modals of the IPMSM have also been drawn on Fig. 18. For example, (0,1) represents that the IPMSM has a 0-order modal in the circumferential direction and a 1-order modal in the axial direction. The vibroacoustic of the IPMSM mainly comes from the radial vibration,

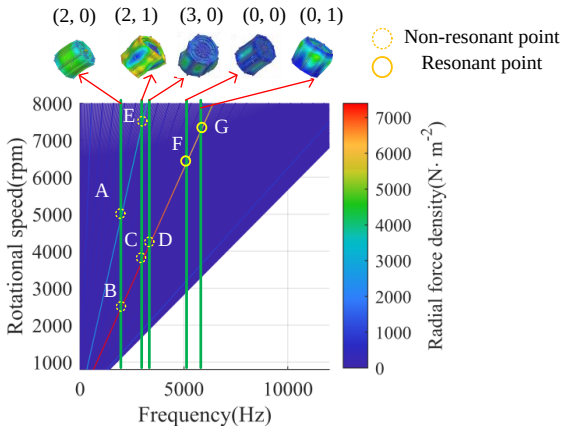

Fig. 18 Unsteady distribution of the electromagnetic force

which is mainly related to the modal in the circumferential direction. It can be seen that the circumferential modals of the IPMSM are mainly 2, 3 and 0, as shown in Fig. 18. According to the spatial order analysis of the electromagnetic force, the lowest non-zero order electromagnetic force of the 8-pole 48-slot IPMSM is 8. Therefore, (2, 0), (2, 1), (3, 0) can be eliminated first. Because there is no electromagnetic force that matches those modal shape. Therefore, resonance do not occur at intersections A-E.

Finally, the zero-order modals contains (0,0) and (0,1), which is a frequency range (5110 Hz-6080 Hz) rather than a fixed and accurate point. Therefore, when the speed is in the range of (6300 rpm-7600 rpm), the frequency is also in the frequency range (5110 Hz-6080 Hz). Moreover, the force shape of the electromagnetic force (0,12f_c) is also the same as the zero-order modals (0,0) and (0,1). Hench, the resonance vibroacoustic s appear in this frequency band and speed range, which are excited by the electromagnetic force (0,12f_c). The diagnostic results provide guidance to reduce IPMSM vibroacoustic from the perspective of excitation source.

5 Experimental Verification

5.1 Current and Magnetic Field Verification

The torque-speed characteristic has been verified the accuracy of the control model in Fig. 7. Further, the experimental currents under the unsteady state are also collected. Time domain and frequency domain distribution are shown in Fig.19 and Fig.20, respectively. In the full speed range, the average error of the fundamental wave amplitude of currents between the simulation and the experimental results is below 4%. The most significant difference is that there is a component $2f_c$ in experimental results under the two working conditions, which is caused by the unbalance of line voltage[20].

Two working conditions at 7100 rpm of acceleration and deceleration are taken as examples. The current waveform and amplitude comparison are shown in Fig. 21.

The electromagnetic FE model is verified through the ultra-thin air gap magnetic field test, which is the method proposed by the authors in the literature[21], as shown in Fig. 22. Hall probe and high-precision workbench are used to test the spatial distribution of open-circuit air gap magnetic field.

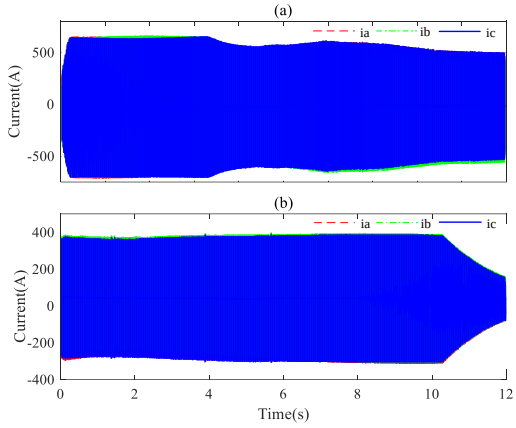

Fig. 19 Experiential results of the stator currents:(a) stator currents under accelerating condition, (b) stator currents under braking condition

The comparison between experimental and simulation results are shown in Fig. 23. The time and frequency domain distribution are in good agreement. The R-square is 90.5%.

5.2 Vibroacoustic Verification

Vibration and noise tests are carried out in the powertrain NVH laboratory with a semi anechoic chamber environment. The background noise of the semi anechoic chamber is 25 dB. The experimental data acquisition hardware/software

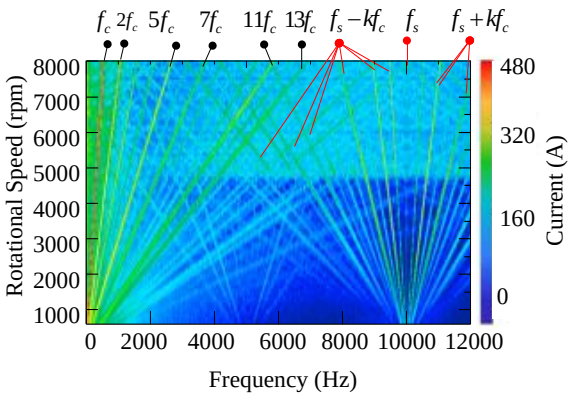

Fig. 20 Experimental results of A-phase current time-frequency diagram: (a) Under accelerating condition, (b) Under braking condition

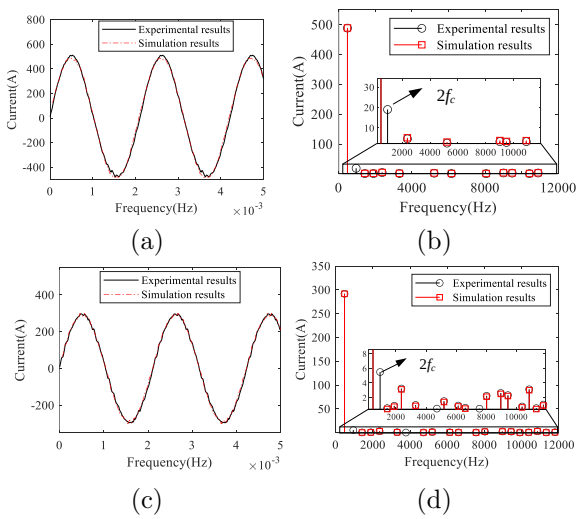

Fig. 21 A-phase current: (a) Time domain results under accelerating condition, (b) Frequency domain results under accelerating condition, (c) Time domain results under braking condition, (d) Frequency domain results under braking condition

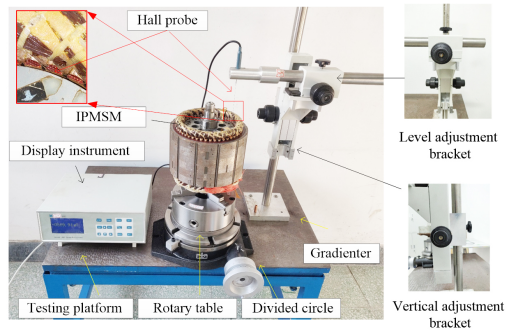

Fig. 22 Test of air gap magnetic field

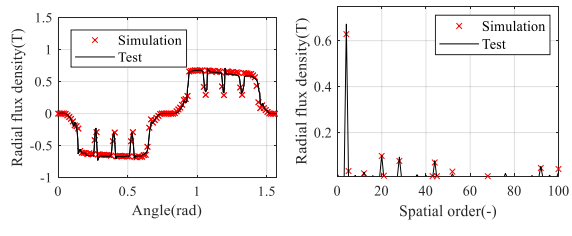

Fig. 23 Spatial distribution and order characteristics of radial magnetic density: (a) Spatial distribution, (b) Order characteristics

equipment mainly includes piezoelectric three-way acceleration sensor, power analyzer, current clamp, LMS 48 channel data acquisition front-end and LMS Testlab acquisition software, as shown in Table 6. The layout of vibration and noise measuring points is shown in Fig. 24. The equipment wiring diagram is shown in Fig. 25

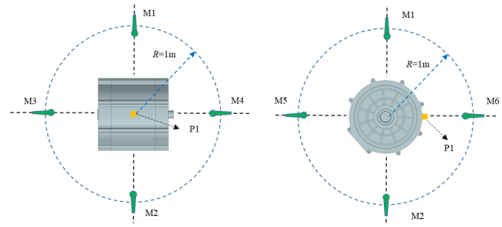

Fig. 24 The layout of vibration and noise measuring points

The test results of vibroacoustic under accelerating and feedback braking conditions are shown in Fig. 26 (a) and (b), respectively. The peak vibroacoustic also appears in the frequency range (5110 Hz-6080 Hz) with the speed range (6300 rpm-7600 rpm).

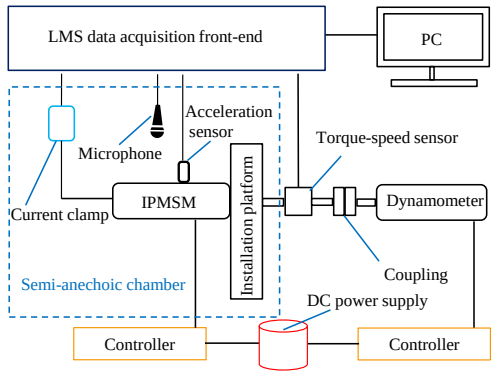

Fig. 25 The equipment wiring diagram

Table 6 Source and characteristics of radial electromagnetic force wave

Name	Model	Number
Acceleration sensors	PCB 356A33	5
Microphones	LMS M31	6
Power analyzer	YOKOGAWA WT3000E	1
Current clamps	YOKOGAWA CT1000	3
LMS data acquisition front-end	SCM 2E09	1
PC	Win10, DELL	1

The results of the overall sound pressure level (SPL) and the $12f_c$ SPL under the acceleration condition are shown in Fig. 27. The results under the feedback braking condition are shown in Fig. 28. In the full speed range, the simulation result has the same trend as the experimental results. However, it is slightly smaller than the test result. The reason is that only electromagnetic vibroacoustic is calculated in the prediction model. The experimental results also contain a lot of mechanical vibroacoustic components.

At the position Xp of maximum vibroacoustic , the $12f_c$ SPL is basically close to the overall SPL. The simulation errors of overall SPL and $12f_c$ SPL during acceleration process are 3.2% and 1.3%, respectively. The simulation errors of feedback braking are 1.5% and 1.1%, respectively.

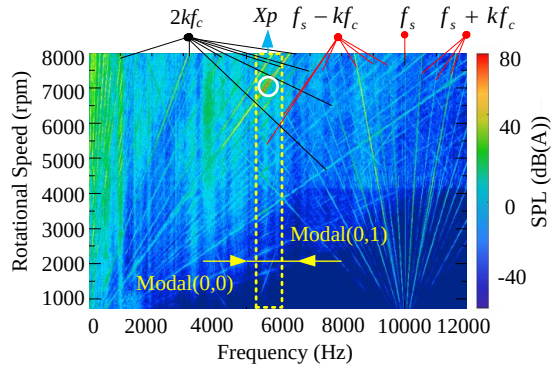

(a)

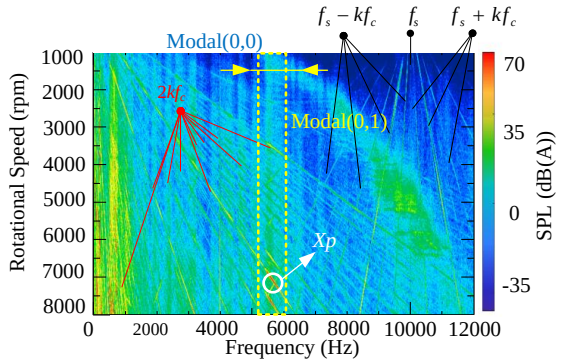

(b)

Fig. 26 Time-frequency diagram of measured vibroacoustic under accelerating condition: (a) Without skewing, (b) With skewing

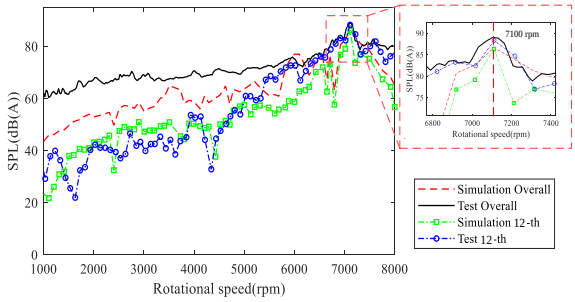

Fig. 27 Test results of vibroacoustic under accelerating condition

6 Conclusions

Considering the rotor step skewing and current harmonics, the prediction and diagnosis of the vibacoustic of ISPMSMs are studied in detail in this paper. Based on variable parameter model of IPMSMs in the control model, segmented mapping of electromagnetic force, the structural FE model with anisotropic material and the ATV method in acoustic calculation, the entire prediction process of unsteady electromagnetic vibroacoustic is efficiently realized at early design stage. The working conditions which are easily excited to resonant vibroacoustic in the unsteady process is diagnosed at early design stage by using predicted results. By analyzing unsteady electromagnetic

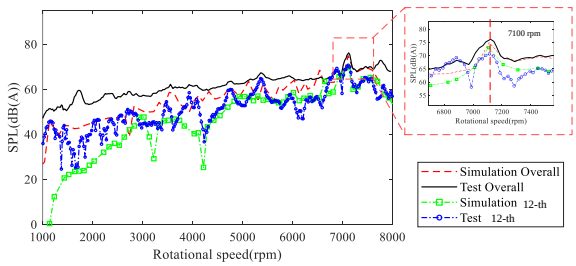

Fig. 28 Test results of vibroacoustic under braking condition

force and simulation modal, the electromagnetic excitation source of resonance vibroacoustic is diagnosed. The proposed method is verified by experiment. The main conclusions are as follows:

- The unsteady electromagnetic vibroacoustic distribution of IPMSMs with step skewing and current harmonics can be predicted accurately. It has been verified by experiments that the amplitude error of the total SPL and the order SPL are both below 3.2% at the operating point of peak vibroacoustic.
- The working conditions which are easily excited to resonant vibroacoustic in the unsteady process are diagnosed in the frequency range (5110 Hz-6080 Hz) with the speed range (6300 rpm-7600 rpm) according to the prediction results. It is also consistent with the experimental results.
- The resonance is excited by (Spatial-zero-order, $12f_c$) electromagnetic force in diagnosed operating conditions.

This study provides guidance for prediction and diagnosis for electromagnetic vibroacoustic performance of IPMSMs under typical unsteady operating conditions.

Acknowledgments. This work was supported by a Grant (Project 51975141) from the National Natural Science Foundation of China.

Declarations

Conflict of Interest. The authors declare that they have no known competing financial interests or personal relationships that could have appeared to influence the work reported in this paper.

References

[1] Zhipeng Wu, Shuguang Zuo, Zhiyong Huang, Xiaorui Hu, Siyue Chen, and Chang Liu. Modelling, calculation and analysis of electromagnetic force and vibroacoustic behavior of integer-slot permanent magnet synchronous motor considering current harmonics. *Journal of Vibration Engineering & Technologies*, 10(3):1135–1152, 2022. https://doi.org/10.1007/s42417-022-00434-x.

[2] C. Ma and S. Zuo. Black-box method of identification and diagnosis of abnormal noise sources of permanent magnet synchronous machines for electric vehicles. *IEEE Transactions on Industrial Electronics*, 61(10):5538–5549, 2014. https://doi.org/10.1109/TIE.2014.2301767.

[3] Shanming Wang, Jianfeng Hong, Yuguang Sun, and Haixiang Cao. Effect comparison of zigzag skew pm pole and straight skew slot for vibration mitigation of pm brush dc motors. *IEEE Transactions on Industrial Electronics*, 67(6):4752–4761, 2019. https://doi.org/10.1109/TIE.2014.2301767.

[4] S. Hu, S. Zuo, M. Liu, H. Wu, and Z. Liu. Modeling and analysis of radial electromagnetic force and vibroacoustic behaviour in switched reluctance motors. *Mechanical Systems and Signal Processing*, 142:106778, 2020. https://doi.org/10.1016/j.ymssp.2020.106778.

[5] Jianbin Liang, James W Jiang, Alan Dorneles Callegaro, Berker Bilgin, Jianning Dong, Debbie Reeves, and Ali Emadi. Prediction of acoustic noise and vibration of a 24/16 traction switched reluctance machine. *IET Electrical Systems in Transportation*, 10(1):35–43, 2020. https://doi.org/10.1049/iet-est.2018.5031.

[6] Qichao Dong, Xintian Liu, Hongzhong Qi, and Yafu Zhou. Vibro-acoustic prediction and evaluation of permanent magnet synchronous motors. *Proceedings of the Institution of Mechanical Engineers, Part D: Journal of Automobile Engineering*, 234(12):2783–2793, 2020. https://doi.org/10.

1177/0954407020919659.

[7] DONG, QiChao, LIU, XinTian, QI, HongZhong, SUN, Chao, WANG, and YanSong. Analysis and evaluation of electromagnetic vibration and noise in permanent magnet synchronous motor with rotor step skewing. *Science China(Technological Sciences)*, v.62(05):133–142, 2019. https://doi.org/10.1007/s11431-018-9458-5.

[8] Xiao Ling, Jianfeng Tao, Bingchu Li, Chengjin Qin, and Chengliang Liu. A multi-physics modeling-based vibration prediction method for switched reluctance motors. *Applied Sciences*, 9(21):4544, 2019. https://doi.org/10.3390/app9214544.

[9] Fu Lin, Shuguang Zuo, Wenzhe Deng, and Shuanglong Wu. Modeling and analysis of acoustic noise in external rotor in-wheel motor considering doppler effect. *IEEE Transactions on Industrial Electronics*, 65(6):4524–4533, 2017. https://doi.org/10.1109/TIE.2017.2758742.

[10] Fu Lin, Shuguang Zuo, Wenzhe Deng, and Shuanglong Wu. Noise prediction and sound quality analysis of variable-speed permanent magnet synchronous motor. *IEEE Transactions on Energy Conversion*, 32(2):698–706, 2017. https://doi.org/10.1109/TEC.2017.2651034.

[11] Shuanglong Wu, Shuguang Zuo, Xudong Wu, Fu Lin, Hongmin Zhong, and Yaodan Zhang. Vibroacoustic prediction and mechanism analysis of claw pole alternators. *IEEE Transactions on Industrial Electronics*, 64(6):4463–4473, 2016. https://doi.org/10.1109/TIE.2016.2645502.

[12] Conggan Ma, Qinghe Liu, Dafang Wang, Qing Li, and Lei Wang. A novel black and white box method for diagnosis and reduction of abnormal noise of hub permanent-magnet synchronous motors for electric vehicles. *IEEE Transactions on Industrial Electronics*, 63(2):1153–1167, 2015. https://doi.org/10.1109/TIE.2015.2481361.

[13] Shuguang Zuo, Fu Lin, and Xudong Wu. Noise analysis, calculation, and reduction of external rotor permanent-magnet synchronous motor. *IEEE Transactions on Industrial Electronics*, 62(10):6204–6212, 2015. https://doi.org/10.1109/TIE.2015.2426135.

[14] Wenzhe Deng and Shuguang Zuo. Analytical modeling of the electromagnetic vibration and noise for an external-rotor axial-flux in-wheel motor. *IEEE Transactions on Industrial Electronics*, 65(3):1991–2000, 2017. https://doi.org/10.1109/TIE.2017.2736487.

[15] Feng Wang, Zhiqiang Wu, and Xiaopeng Li. Analytical modelling of radial coupled vibration and superharmonic resonance in switched reluctance motor. *Journal of Vibration Engineering & Technologies*, 9(3):449–467, 2021. https://doi.org/10.1007/s42417-020-00238-x.

[16] Xiaoqiang Guo, Rui Zhong, Mingshu Zhang, Desheng Ding, and Weifeng Sun. Fast computation of radial vibration in switched reluctance motors. *IEEE Transactions on Industrial Electronics*, 65(6):4588–4598, 2017. https://doi.org/10.1109/TIE.2017.2767548.

[17] Xiaoyuan Wang, Xibin Sun, and Peng Gao. Study on the effects of rotor-step skewing on the vibration and noise of a pmsm for electric vehicles. *IET Electric Power Applications*, 14(1):131–138, 2020. https://doi.org/10.1049/iet-epa.2019.0238.

[18] Xiaoyong Zhu, Zixuan Xiang, Li Quan, Wenye Wu, and Yi Du. Multimode optimization design methodology for a flux-controllable stator permanent magnet memory motor considering driving cycles. *IEEE Transactions on Industrial Electronics*, 65(7):5353–5366, 2017. https://doi.org/10.1109/TIE.2017.2777408.

[19] Aryanti Kusuma Putri, Sebastian Rick, David Franck, and Kay Hameyer. Application of sinusoidal field pole in a permanent-magnet synchronous machine to improve

the nvh behavior considering the mtpa and mtpv operation area. *IEEE Transactions on Industry Applications*, 52(3):2280–2288, 2016. https://doi.org/10.1109/TIA.2016.2532289.

[20] Jacek F Gieras, Chong Wang, and Joseph Cho Lai. *Noise of polyphase electric motors*. CRC press, 2018. https://doi.org/10.1201/9781420027730.

[21] Conggan Ma, Shengsen Zhou, Na Yang, Michele Degano, Christopher Gerada, Jianguang Fang, and Qinghe Liu. Characteristic analysis and direct measurement for air gap magnetic field of external rotor permanent magnet synchronous motors in electric vehicles. *IET Electric Power Applications*, 14(10):1784–1794, 2020. https://doi.org/10.1049/iet-epa.2019.0931.